Inhomogeneous Schwarz Diamond Lattice Structures for Load-Bearing Orthopedic Implants: Fabrication and Mechanical Evaluation

Fatemeh Zarei[1], Aziz Shafiei-Zarghani*[2,3]

1 Department of Materials Science and Engineering, School of Materials and Civil Engineering, Shiraz University, Shiraz, IRAN.

2 Department of Materials Science and Engineering, School of Materials and Civil Engineering, Shiraz University, Shiraz, IRAN. a3shafiei@gmail.com, ashafiei@shirazu.ac.

3 Additive Manufacturing Department, Mehrawin, Shiraz, IRAN.

Acknowledgements

We would like to express our sincere gratitude to the funding sources of this research project, including Shiraz University, Shiraz3D Technology center for digital manufacturing, and Mehrawin Co. Their financial support was essential in conducting this study and achieving its outcomes. Additionally, we would like to extend our appreciation to the pre-clinical laboratory of Tehran University of Medical Sciences for providing access to their Micro-Computed Tomography (Micro-CT) test machine, which enabled us to obtain crucial data for this research. We also thank all the individuals who contributed to this project through their support, guidance, and technical assistance.

Competing Interest

Statements and Declarations

The authors report there are no competing interests to declare.

This work was supported by the Shiraz University; and the Mehrawin Shiraz Co.

Abstract:

This study explores the design, fabrication, and mechanical evaluation of inhomogeneous Schwarz diamond lattice structures intended for use in load-bearing orthopedic implants. These lattice structures were created using the selective laser melting (SLM) process, with pore sizes varying from 500 to 2000 μm. To assess their geometrical accuracy and mass transport capabilities, a series of evaluations, including micro-CT analysis, density measurements, and permeability tests, were performed. The mechanical tests revealed that the fabricated structures exhibited ductile behavior, showcasing excellent strength and stiffness, particularly in two groups of lattices with higher porosity levels. The irregular distribution of pore sizes in these lattices led to an ideal bending-dominated behavior for stiffness and a stretch-dominated behavior for strength. These findings indicate that the inhomogeneous Schwarz diamond lattice structures hold significant promise as micro-architected implants. Their high strength-to-stiffness ratio makes them particularly suitable for orthopedic applications, where such characteristics are crucial for effective load-bearing performance. This research highlights the potential of using advanced lattice designs to improve implant functionality and integration with host tissues.

Keywords: Schwarz diamond lattice, Orthopedic implants, Additive manufacturing, Selective laser melting (SLM), Micro-architected implants

1 Introduction:

Orthopedic surgeries have become increasingly common due to the rising incidence of diseases such as trauma, tumor, and osteoarthritis, among others (Murr et al., 2009; Nakamura et al., 1985; Sanli et al., 2016). However, implant failure and bone resorption remain major challenges, particularly due to the phenomenon of stress shielding. Stress shielding occurs when the stiffness of an implant is higher than that of the surrounding bone, leading to a reduction in load-induced stimulus for bone regeneration and, ultimately, implant failure. Therefore, there is a critical need to minimize stress shielding to enhance implant durability. One approach is to reduce the young modulus of the implant to match the stiffness of the injured bone without compromising its load-bearing ability (Arabnejad et al., 2016; Gibson and Ashby, 2014a; Insua et al., 2017; Leng et al., 2019; Pobloth et al., 2018; Taniguchi et al., 2016). Porous implants are particularly promising in this regard, as they can reduce stress shielding and achieve a closer mechanical match with natural bone compared to non-porous implants (Liu et al., 2021; Ridzwan et al., 2007).

The internal structure of an implant plays a critical role in controlling new bone and cartilage formation. In load-bearing applications, the implant must also facilitate the skeletal reconstruction of bone defects, which remains a major challenge. To optimize the implant, its porous structure should possess pore interconnectivity, which enables cell ingrowth and nutrient and waste transfer implant (Hutmacher, 2000; Jones et al., 2009; Loh and Choong, 2013). To achieve this, different lattice structures have been designed; however, the complexity of their structures has limited the use of many fabrication methods, including conventional ones. Additive Manufacturing (AM) is a promising production technique that enables the construction of complex geometries with controlled architectures. The key to the success of this method is its layer-wise construction strategy, which involves a direct connection with the previously designed computer-aided (CAD) model. In recent years, the capabilities of AM methods have advanced significantly, leading to the design and fabrication of various micro-architected implants with complex lattice structures.

Triply Periodic Minimal Surfaces (TPMS) are a new generation of complex conceptual geometries which have been employed as the internal architecture of porous implants. Because of their geometry, they represent a new set of wonderful properties besides the ones mentioned above. Of these new properties, it can be mentioned that the surface of TPMS topologies has a zero-mean curvature with a vast area, which results in higher-rated cell growth (Al-Ketan and Abu Al-Rub, 2019; Dong and Zhao, 2021; Ma et al., 2020; Zarei et al., 2023). Furthermore, Dong and Zhoa showed that the TPMS structures have a high degree of pore interconnectivity that provides spaces for nutrient and waste transportation, facilitating vascularization and cell ingrowth. This characteristic is in direct proportion to the biological stabilization of the implants (Dong and Zhao, 2021). There have been numerous studies to investigate the manufacturability and mechanical performance of different TPMS structures in recent years. Most early studies have been worked on the Schwarz Gyroid structure as it poses wonderful manufacturability. In addition, Gyroid showed robust mechanical properties such as high compression and tensile strength and high effective shear modulus (Ataee et al., 2018; Barba et al., 2019; Jones et al., 2009; Lu et al., 2020; Yan et al., 2015; Yu et al., 2020). Neovius is another example that outperforms some other famous structures in terms of stiffness, strength, and energy absorption (Abueidda et al., 2019; Rezapourian et al., 2021). As a potential structure of the TPMS family, Schwarz Diamond has demonstrated special capabilities. Novak and coworkers showed that the Diamond lattice structure made of 316L alloy exhibits the highest energy absorption compared to other structures of Gyroid, Schwarz Primitive, and IWP (Novak et al., 2021). Or in another research Guo et al., revealed that Diamond has the highest surface area among Gyroid, Primitive, and IWP (Guo et al., 2019). However, while the Diamond structure has represented promising characteristics, based on the literature, still a lack of research on its properties can be felt.

Despite the extensive research on various types of TPMS structures, including Gyroid and Diamond, most studied structures have been regular in dimensions. However, irregular structures have shown promise in achieving enhanced mechanical behavior and mass flow properties. Recent research has suggested that irregular structures may offer even greater potential for achieving optimized mechanical behavior and mass flow properties. For instance, studies have shown that irregular lattices can exhibit unique mechanical properties, such as enhanced strength and toughness, due to their ability to distribute stresses more uniformly throughout the structure (Pan et al., 2020; Zhou et al., 2019). In light of these findings, investigating the properties of irregular TPMS structures is an important step towards advancing the field of porous implant design. In this work, we aim to investigate an irregular structure and its effects on these properties, providing a novel approach to achieving a higher strength-to-stiffness ratio in porous implants. By studying such an irregular structure, we hope to contribute to the broader understanding of porous implant design and provide insights that could inform the development of more effective and efficient implants.

2 Materials and Methods

2.1 Design and Fabrication

The Schwarz Diamond TPMS structure for three different groups of samples was designed using Rhinoceros 7 software and a Grasshopper plugin based on its mathematical equation, as shown in Formula (1):

$$\sin(ax)\sin(by)\sin(cz) + \sin(ax)\cos(by)\cos(cz) + \cos(ax)\sin(by)\cos(cz) + \cos(ax)\cos(by)\sin(cz) = 0 \quad (1)$$

The constants a, b, and c were varied to determine the size of pores in the architected structures. Table 1 provides the nominal pore sizes for each sample group. The models were modified and prepared for 3D printing using Autodesk Netfabb Ultimate 2021 software. The overall shape of all 3D models was determined to be cylindrical with a diameter of 6 mm and a height of 12 mm based on ISO 13314 instructions.

For the manufacturing of samples, gas atomized 316L powder (<65µm) with a chemical composition of C ≤ 0.03%, Mn ≤ 2%, Cr 16–18%, Si ≤ 1.00%, P ≤ 0.045%, S ≤ 0.030%, Ni 10–14%, Mo 2.00-3.00%, and Fe-Bal. was used. SLM fabrication was performed in an argon atmosphere using a NOURA M100P SLM machine. The machine's maximum laser power was 300 W, build time was 1.5 h, layer thickness was 30 µm, and volume building rate was 8-18 cm^3/h. The build orientation was parallel to the axis of the samples, and Figure 1 shows the produced samples with their corresponding coordinate axes. After the samples were removed from the platform by wire cutting, they were post-processed with sand blasting and cleaned with ultrasonic.

Table 1- Nominal pore sizes of the sample groups fabricated using SLM technique.

Sample group	Nominal pore size 1, µm	Nominal pore size 2, µm
S1	500	1000
S2	1000	1500
S3	1500	2000

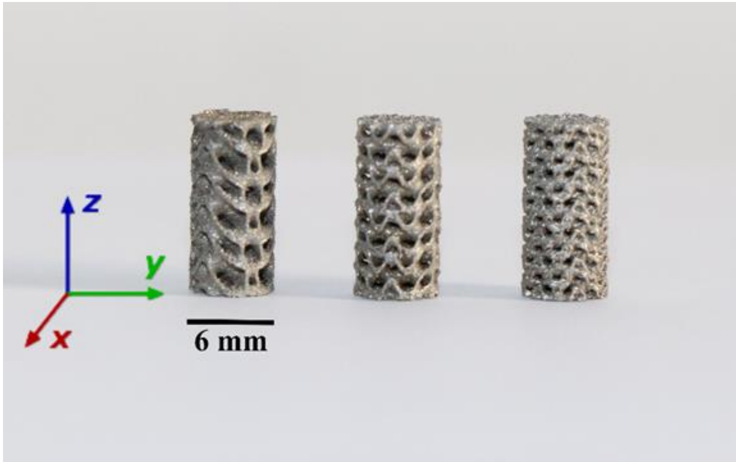

Figure 1. Photograph of the fabricated lattice structures with varying pore sizes used in this study.

2.2 Measurements

In this section, the measurement methods used to analyze the Diamond structure's properties are described. To avoid confusion, the authors differentiate between "porosity," referring to the interconnected microchannels within the Diamond structure, and "voids," referring to the closed internal micro-pores that form during the manufacturing process. The authors used a Micro-Computed Tomography scanner (Micro CT, LOTUS in Vivo) to analyze surface appearance, pore size accuracy, channel connectivity, and manufacturing imperfections. The X-ray tube voltage and current were set to 90 kV and 58 µA, respectively, with a frame exposure time of 2 seconds at 2.1 magnification. Avizo Lite 2019 software was used to rebuild 3D models of the samples from the 2D slice images.

The density measurements were carried out using Archimedes' method, with the possibility of calculating the percentage of porosities and voids. Samples were immersed in alcohol for 2 hours, and their densities were calculated using the equation provided in the text. The percentage of voids and porosities was calculated using the following equation (Yánez et al., 2018):

$$\rho_i = \left(\frac{\rho_{alc} \times W_a}{W_a - W_{alc}}\right) \tag{2}$$

Where ρ_{alc} and W_{alc} are respectively the weights of implants in air and alcohol. These measurements repeated three times. Then, the percent of voids computed as below:

$$P_v = \left(1 - \frac{\rho_i}{\rho_d}\right) \times 100 \tag{3}$$

Where ρ_d is theoretical bulk density of *316L* (7.98 g/cm^3). The percent of porosities can also be calculated as follow:

$$P_p = \left(1 - \frac{(\frac{W_a}{V})}{\rho_d}\right) \times 100 - P_v \quad (4)$$

Where V is the overall cylinder volume of implants.

Permeability was measured using the Falling Head method. In this method, the sample is fixed at the end of a standpipe, and water is poured into the pipe. Figure 2 shows a schematic of the setup for the Falling Head method. The period it takes for the water to reach from height L1 to L2 is recorded, and the permeability of each sample is assessed using Darcy's law, with the respective following formulas (Pennella et al., 2013).

$$k = K\mu/\rho g \quad (5)$$

Where ρ is density of water, g is gravity, μ is dynamic viscosity coefficient of water, and K is hydraulic conductivity, which its equation is as follow:

$$K = \frac{aH}{A(\Delta t)} \ln(\frac{L_1}{L_2}) \quad (6)$$

Where "H" is the height of implant, and "a" and "A" are the cross-section areas of stand pipe and implant, respectively.

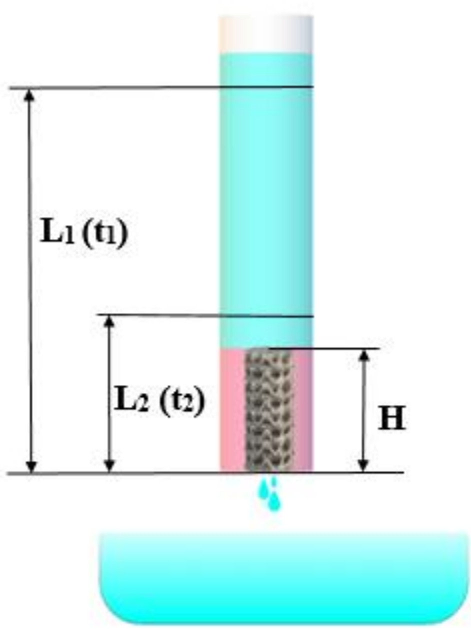

Figure 2. Schematic illustration of the Falling Head method setup for permeability measurement.

2.3 Microstructural Studies

To prepare the samples for microstructural studies, a series of steps were followed to ensure optimal observation. Firstly, the samples were wire cut, mounted, and ground using SiC papers up to #2000. The polished samples were then subjected to electro etching for 7 seconds in a solution of 10 g oxalic acid and 90 mL water with a voltage of 10 V. The optical microscope (OM) used was Dino Eye AM 423X to observe and characterize the morphology, microscopic aspects, and strut thickness of the structures. For finer details, the surface morphology of the as-built samples and microstructure of the electro-etched ones were examined using a Scanning Electron Microscope (SEM), specifically a VEGA3 TESCAN. These steps were taken to ensure that the microstructural analysis was carried out with precision and accuracy.

2.4 Mechanical Characterization

To investigate the mechanical behavior of the samples, compression tests were conducted at room temperature in accordance with ISO 13314 standard, using a universal testing machine with a constant crosshead speed of 0.5 mm/min. The load was applied along the Z-axis until a displacement of 9 mm was reached, and the load-displacement curves were recorded. Based on these curves, the engineering stress (σ)-strain (ε) curve, stiffness (E), and yield strength (σy) were determined for each sample. Three samples were tested for each structure, and the average values were presented. In addition, compression tests were simulated using SimSolid software to investigate the deformation mechanisms and determine stress concentration areas.

3 Results and Discussion

3.1 Physical Properties

In Fig. 3, the 3D renderings of the samples' structures reconstructed by Micro-CT data are compared to the CAD models. The distribution of pore and strut sizes obtained from the segmentations of Micro-CT results are shown graphically in Fig. 4. For all three groups of samples, it is evident that the histograms of the strut sizes are symmetric and unimodal with short ranges and with no outliers. In the case of pore sizes, the histograms demonstrate a bimodal distribution, which represents two distinct groups of designed pore sizes. However, by increasing the porosity from S1 to S3 groups, the peaks shift closer together, and the histograms become more uniform. This indicates lowering the structural irregularity from S1 to S3 samples. The average values of the pore sizes and representative designed values are shown in Table 2. This table also lists the porosity percent calculated using density measurements and Micro-CT results beside the designed values. The data indicates that the pore sizes of the as-built samples are slightly decreased, unlike the strut sizes that consistently increased. There is also a slight trend of higher manufacturing accuracy towards the samples with larger pore sizes. However, this trend is not statistically significant. These geometrical deviations are negligible, and it can be said the samples are produced with reasonable geometrical accuracy. The SEM images taken from the top surfaces of samples in Fig. 3 also reveal the manufacturing accuracy. The dimensional mismatching is attributed to the local instabilities in the melt pools, which occur during the scanning of the laser across the powder bed. As a matter of fact, the melt pools could become unstable due to Marangoni or thermo-capillary flow, which is attributed to the rapid convective motion of melted powders (Gu et al., 2013; Lee et al., 1998; Rombouts et al., 2006; Yadroitsev et al., 2007).

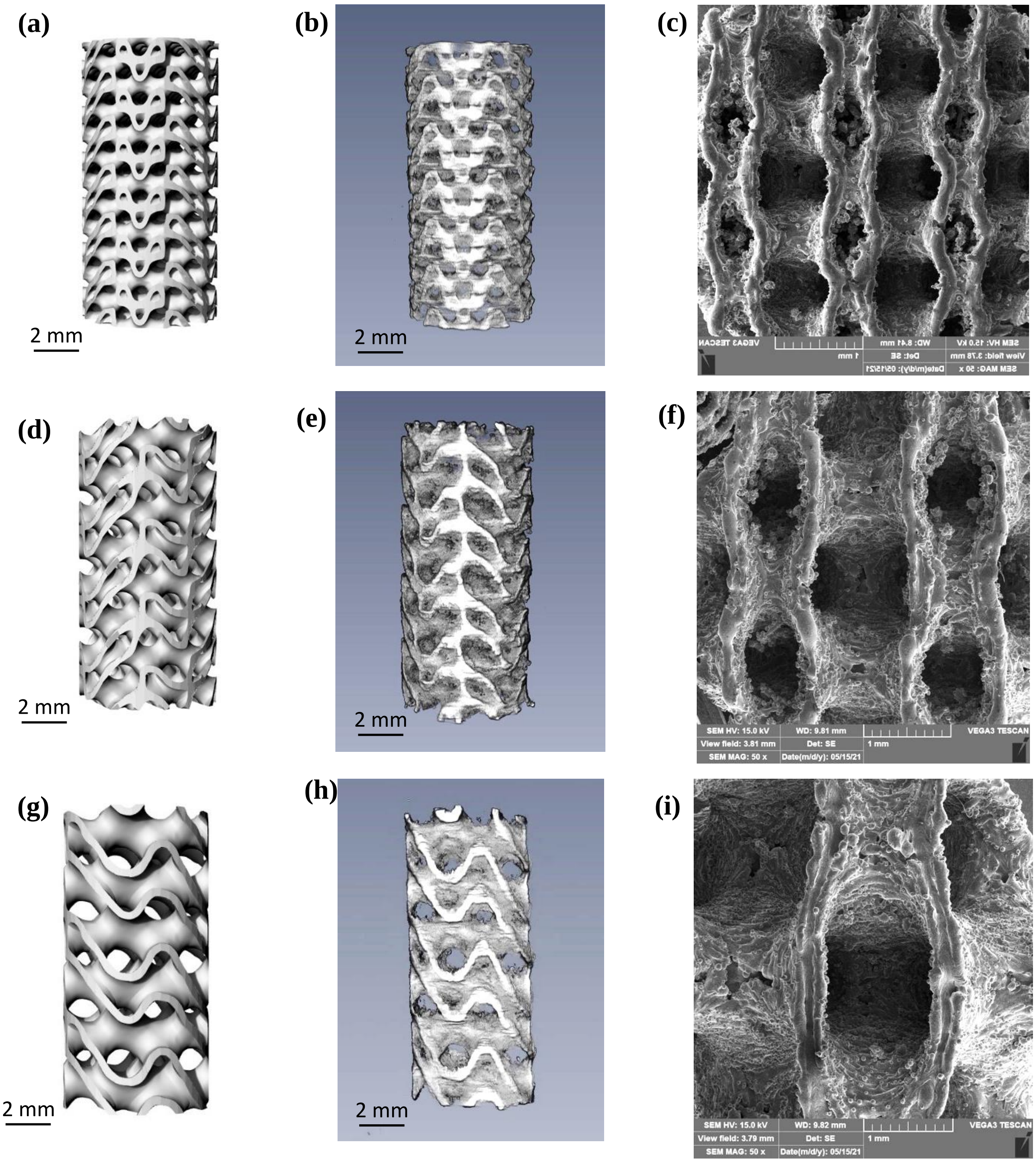

Figure 3. Comparison of designed CAD models (a, d and g) with 3D constructed models obtained from Micro-CT data (b, e and h) and representative SEM micrographs (c, f, and i) for S1, S2, and S3 samples, respectively.

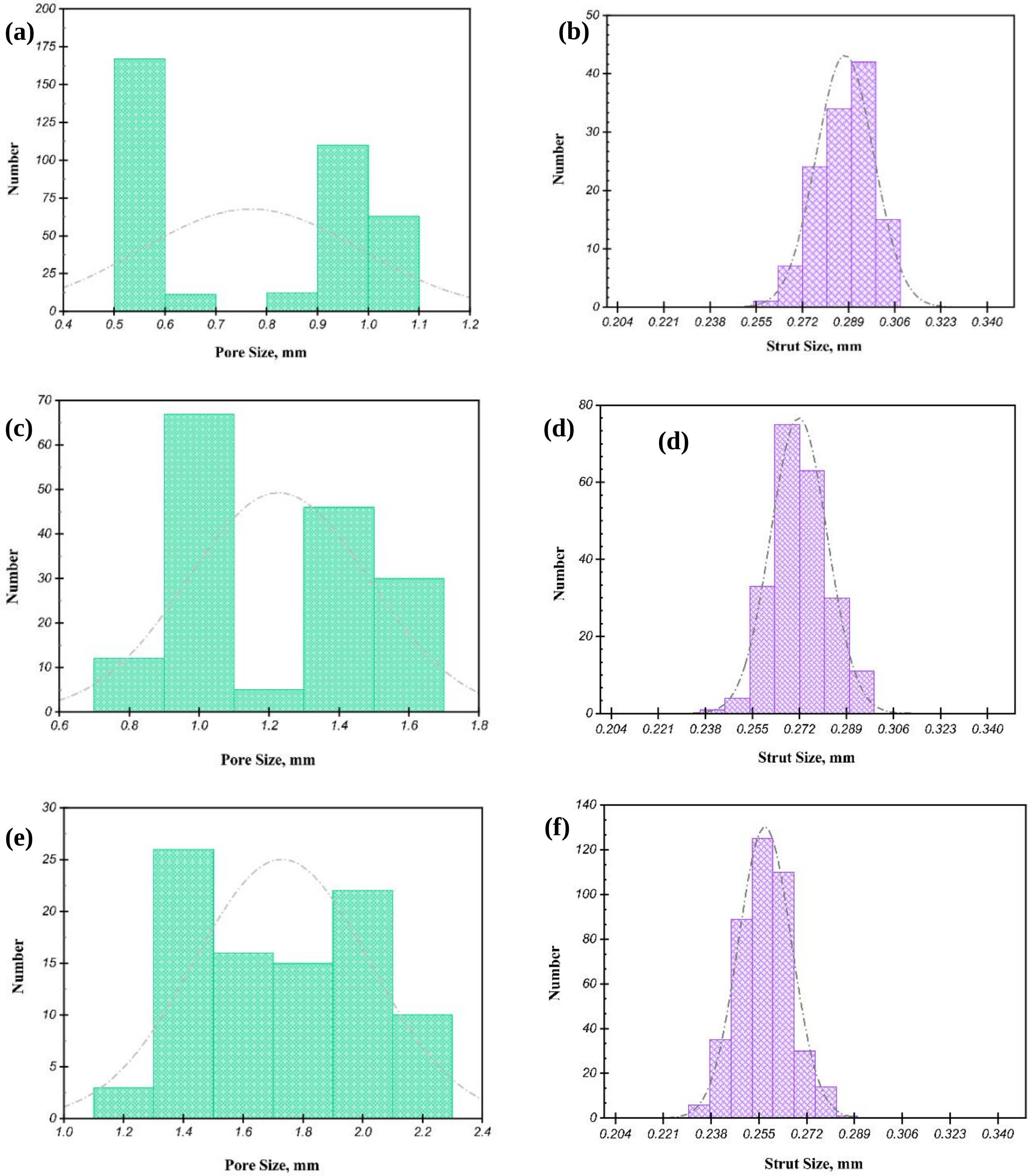

Figure 4. Histograms presenting the distribution of pore size and strut size for the S1 (a-b), S2 (c-d), and S3 (e-f) lattice structures.

Table 2- Geometrical data of each sample group including the designed and computed parameters.

Sample	Porosity, % (Deviation from CAD, %)			Strut Size, um (Deviation from CAD, %)		Pore Size, um (Deviation from CAD, %)		Permeability, m^2
	CAD	uCT	Density	CAD	uCT	CAD	uCT	
S1	52.5	50.1 (-4.6)	56.7 (8.0)	250	287.7 (15.1)	500 1000	556.8 (11.4) 978.5 (-2.2)	$4.1 * 10^{-10}$
S2	73.1	68.8 (-5.9)	64.3 (-12.0)	250	269.5 (7.8)	1000 1500	976.7 (-2.3) 1472.4 (-1.8)	$5.6 * 10^{-10}$
S3	76.2	74.6 (-2.1)	70.1 (-8.0)	250	258.2 (3.3)	1500 2000	1441.7 (-3.9) 1978.7 (-1.1)	$7.7 * 10^{-10}$

The permeability of the implants is an important parameter that influences the efficacy of bone ingrowth. Low permeability can lead to inadequate nutrient supply and waste removal, while excessive permeability can compromise the mechanical integrity of the implants and result in cell washout washout (Bobbert and Zadpoor, 2017; Karageorgiou and Kaplan, 2005). Therefore, designing the structural features of the implants to achieve an optimum permeability is crucial. This optimum value is dependent on the pore size, porosity, and architecture of the implants (Cartmell et al., 2004). For trabecular bone, the permeability range varies from 0.4×10^{-9} to 11×10^{-9} m^2 (Grimm and Williams, 1997). In this study, the calculated permeability values for all three groups of samples, as presented in Table 2, are consistent with this range. Additionally, the permeability coefficients were found to increase with increasing porosity, as larger pores and a straight-through connecting geometry offer less resistance to fluid flow. Therefore, the designed structural features of the implants in this study are expected to promote efficient bone ingrowth while maintaining their mechanical integrity.

3.2 Microstructural Characteristics

In this study, the microstructural characteristics of the samples were examined using optical microscopy. The OM images in both horizontal and vertical cross-sections for all groups of samples are presented in Fig. 5. The molten pools, which are the characteristic of the SLM procedure, can be observed in the images. The overlap of these molten pools is due to the successful fusion of particles and bonding in each layer (Ahmed et al., 2022). It can be seen that there is no clear difference in the shape and size of molten pools among the samples. However, significant differences between the scan direction (horizontal cross-section) and build direction (vertical cross-section) can be observed.

In the planes parallel to the build direction, curved fish scale-like molten pools are formed due to the partial re-melting of sequentially deposited layers that have been solidified (Lore et al., 2013). Additionally, all samples are dominated by many columnar grains contained within some molten pools. Each grain is characterized by a fine cellular structure that grows along a single orientation (Fig. 6). This fine microstructure has occurred due to rapid solidification and a high cooling rate during the SLM procedure. Laser melting causes high local cooling rates, resulting in directed solidification and extremely fine grains called sub-grains. This fine microstructure improves the mechanical properties of the samples. There have been numerous studies that have shown the relationship between fine microstructure and improved mechanical properties in various metallic alloys. For example, research on Ti-6Al-4V alloy has shown that a fine microstructure with sub-micron grain sizes results in improved mechanical properties such as higher yield and tensile strength, as well as improved fatigue and fracture toughness (Meng et al., 2022; Nguyen et al., 2022).

However, some holes or poor fusion can be observed in the boundary of molten pools (marked by purple circles in Fig. 5). This is because the laser heat is mostly concentrated in the center of the melt pool, and the edge receives lower heat. Moreover, a few voids observed in the images are in close correlation with the results of density measurements in Table 2. These observations provide insights into the microstructural characteristics of the samples and can help in optimizing the SLM process parameters for better quality products.

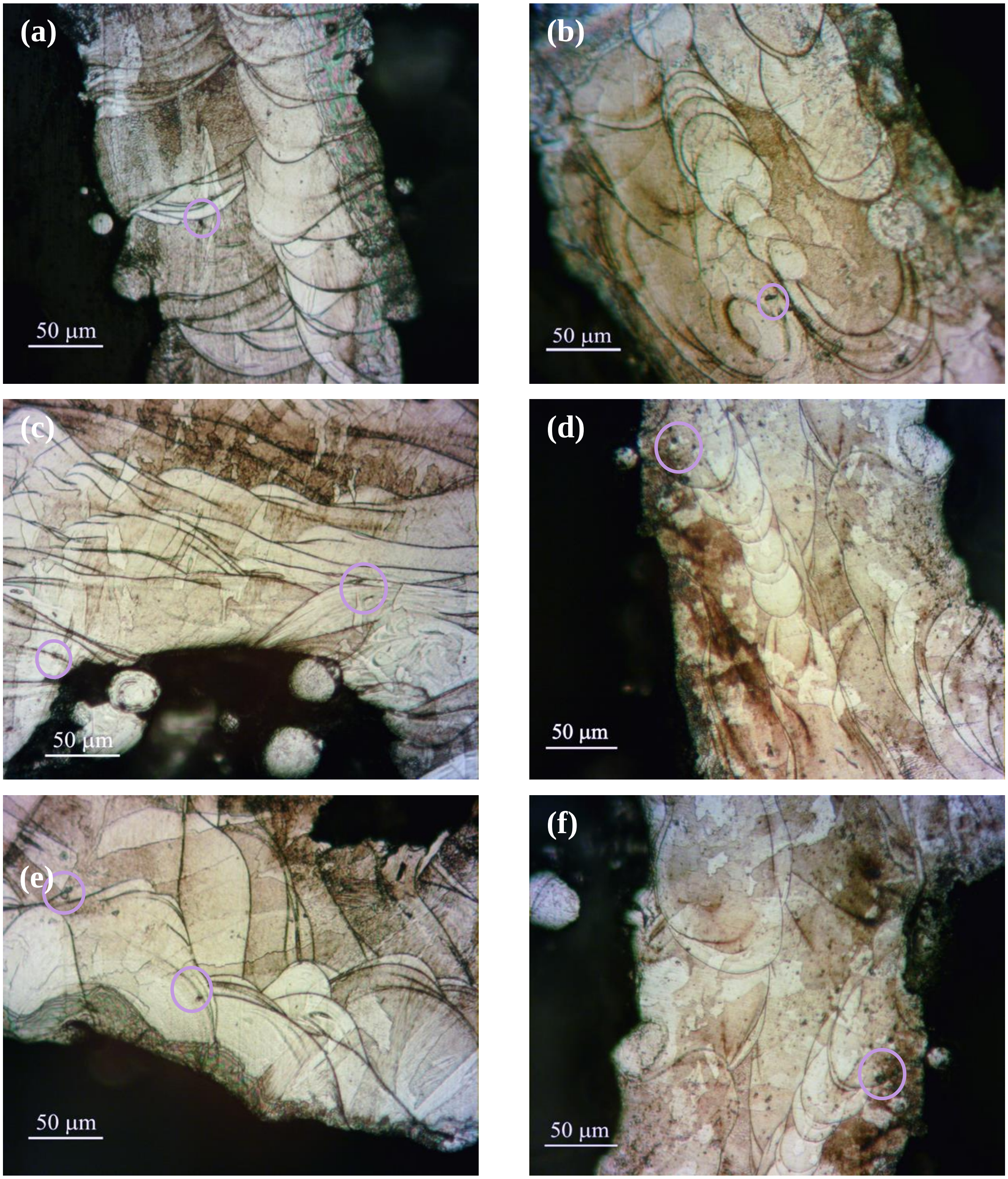

Figure 5. Optical microscopy images showing the microstructure of vertical and horizontal cross-sections of the fabricated lattice structures: (a-b) S1, (c-d) S2, and (e-f) S3. The purple circles highlight the voids formed during the fabrication process.

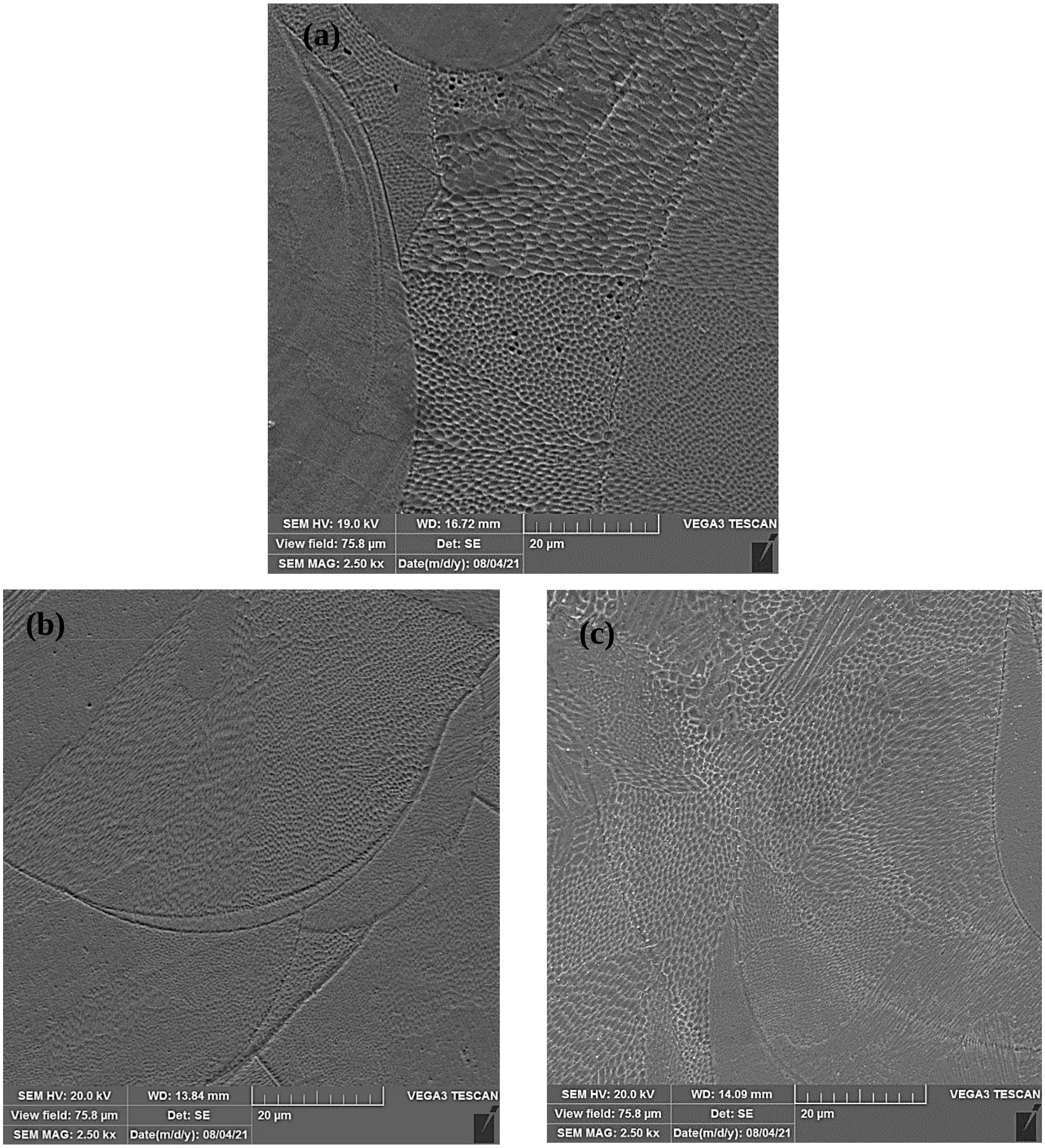

Figure 6. SEM micrographs depicting the melt pools and sub-grains of the fabricated lattice structures: a) S1, b) S2, and c) S3 samples.

3.3 Mechanical Performance

The mechanical properties of the samples were evaluated by analyzing their stress-strain curves under uniaxial compressive loading, as shown in Fig. 7. The curves display the typical compressive behavior of ductile cellular solid structures. The initial linear elasticity region is attributed to the bending and elastic buckling of the struts. The onset of plasticity truncates this region, leading to the second regime, the plateau stage, which is primarily controlled by the crushing of the structure and the formation of plastic hinges. The smooth and nearly constant stress values in this region represent the ductile behavior of the samples. The third stage, called the densification region, is where the stress increases steeply. This effect is purely geometric, resulting from the impingement of the opposite struts, which are forced into contact, and further bending is not possible (Ashby, 2005; Cheng et al., 2012; Gibson and Ashby, 2014a). The presence of a fine cellular microstructure in the samples, as discussed in section 3.2, has a significant effect on their mechanical properties. Previous research has shown that a fine microstructure leads to increased strength and improved ductility in cellular solids (Aboulkhair et al., 2019).

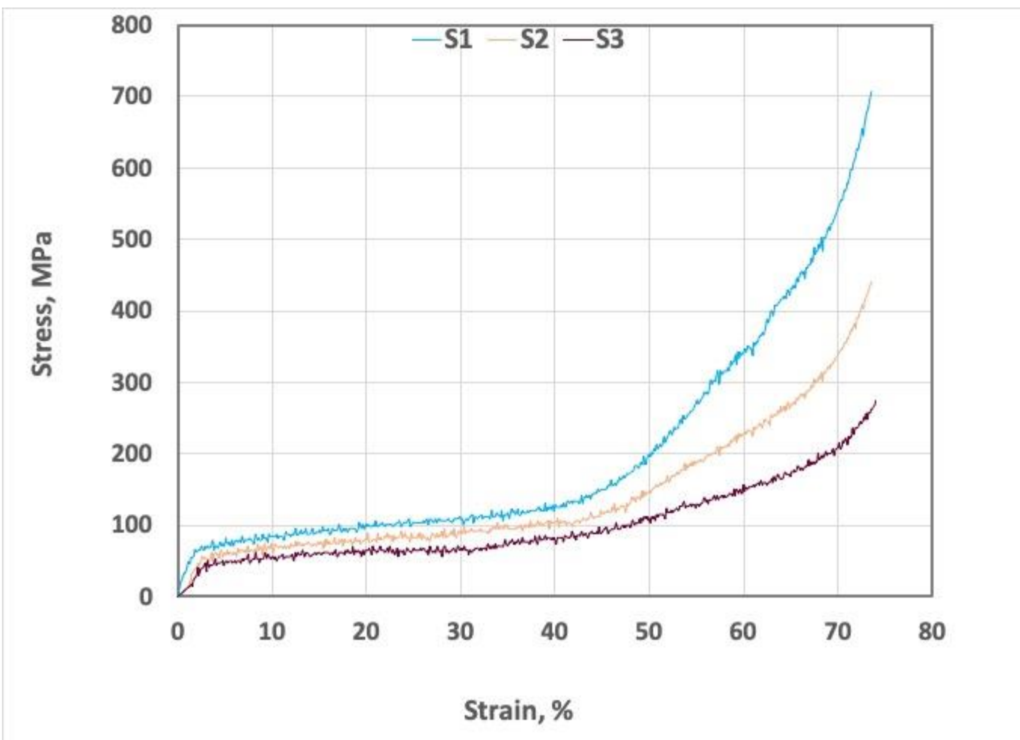

Figure 7. Uniaxial compressive stress-strain curves for irregular TPMS Diamond lattice structures with pore sizes ranging from 500 to 2000 μm, showing their mechanical performance under loading.

The mechanical performance of the cellular solid structures was evaluated through the slope of the elastic region, which represents their stiffness. The stiffness values obtained for the S1, S2, and S3 samples were 20.5, 13.7, and 11.4 GPa, respectively, demonstrating a significant decrease of 89%, 93%, and 94% from the dense 316L alloy (193 GPa). However, it is important to note that the mechanical properties of human bone vary depending on age and location, with trabecular bones in the proximal tibia and femur exhibiting stiffness values of 11.4 and 13.0 GPa, respectively (Ashman and Jae Young Rho, 1988; Townsend et al., 1975). Thus, the stiffness values achieved in the present study, particularly for samples S2 and S3, fall well within the range of trabecular bone stiffness.

The 0.2% offset yielding stresses for samples S1, S2, and S3 were found to be approximately 79, 62, and 47 MPa, respectively. Compared to the yielding strength of trabecular bone, which typically ranges from 3-30 MPa (Wang et al., 2016), all of the fabricated structures exhibited reasonable strength with a good safety factor. These findings indicate that the cellular solid structures have mechanical properties that are suitable for biomedical applications, particularly in situations where the implant material should match the mechanical properties of the surrounding bone.

The cross-sectional analysis of the deformed samples, and the stress distribution predicted by the simulation depicted in Fig. 8. These analyses indicate similar deformation characteristics among all samples, with a strong correlation between the high-stress areas and the location of plastic hinges (Ataee et al., 2018). In uniaxial compression, the horizontal struts carry tensile loading, while the vertical arms are loaded in compression. The deformation initially occurred in the form of elastic bending and buckling of vertical struts, while the horizontal struts bear tensile loads and support the unit cell. Smaller unit cells remained intact, while larger ones underwent significant deformation, with their struts impinging together. Smaller unit cells demonstrated stronger performance, while larger ones contributed to better stiffness. A more thorough understanding of this behavior can be attained through quantitative investigation of the structure’s performance, as follows.

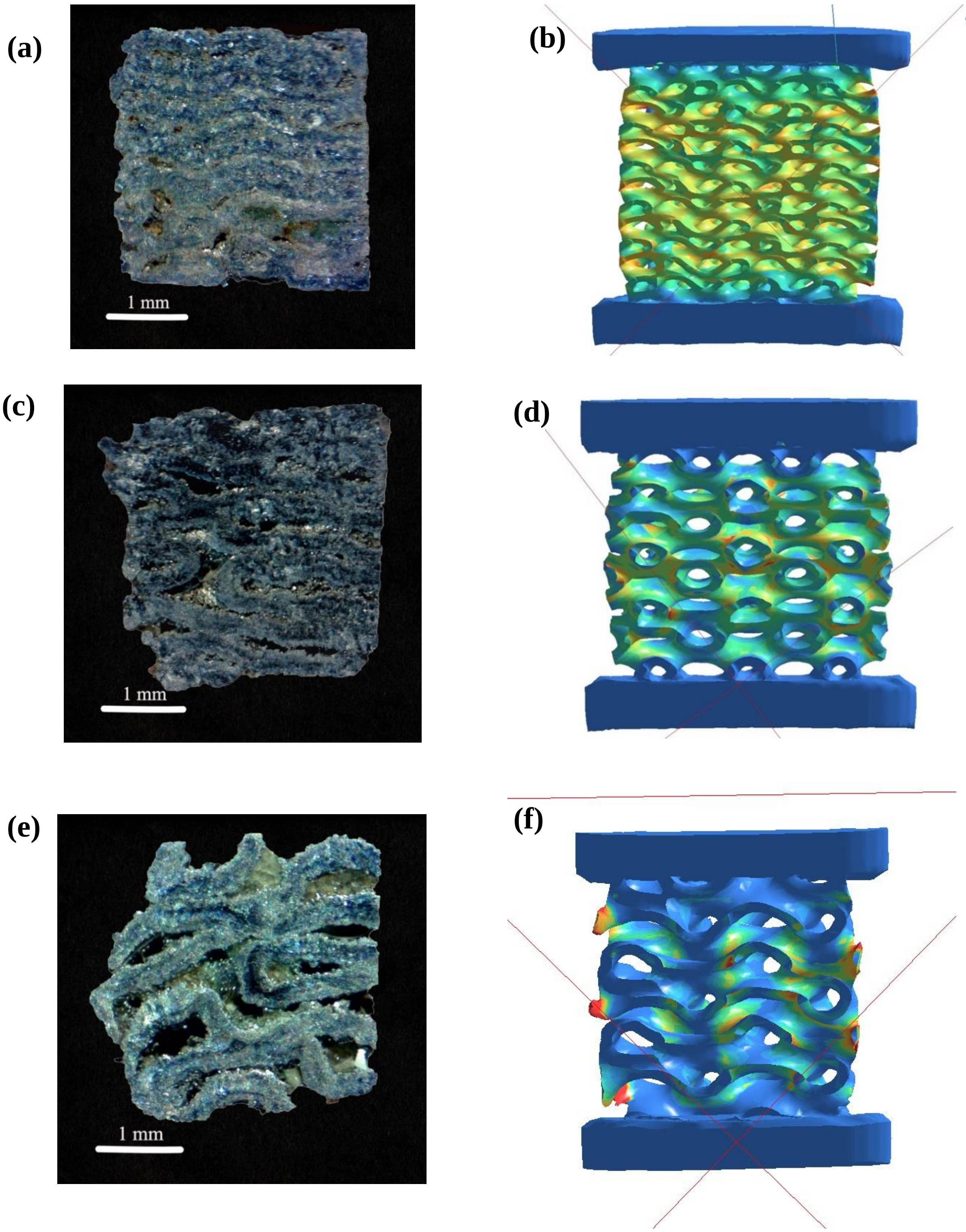

Figure 8. Cross-sectional views and corresponding stress distributions predicted by simulations for a) and b) S1, c) and d) S2, and e) and f) S3 lattice structures under uniaxial compression.

The mechanical performance of lattice structures is highly dependent on their topology, relative density, and the manufacturing material (Maconachie et al., 2019). Thus, the mechanical properties of cellular structures are often presented as relative properties, which are calculated by dividing the values of the structure by those of the solid material. The relative modulus and strength can be calculated using the following formula:

$$E^* = E_c/E_s \quad (7)$$

$$\sigma^* = \sigma_c/\sigma_s \quad (8)$$

Where E and σ represent modulus and strength, respectively, while * denotes "relative", c denotes "cellular solid", and s denotes "solid". The relationship between these two characteristics and relative density (ρ*) (solid fraction of samples) can be defined as follows:

$$E^* = C_1(\rho^*)^n \quad (9)$$

$$\sigma^* = C_2(\rho^*)^m \quad (10)$$

where C1 and C2 are constants, and n and m are determined by the structural features and represent the slopes of logarithmic values of E* and σ* versus relative density (Gibson and Ashby, 2014a). Two types of ideal cellular designs can be distinguished based on equations 9 and 10: stretch-dominated and bending-dominated. The stretch-dominated design is extremely stiff and strong for a given relative density, whereas the bending-dominated design has high energy absorption capacity but lower structural efficiency and strength (Ashby, 2005; Gibson and Ashby, 2014b). The locus of relative stiffness and strength against relative density for ideal stretch- and bending-dominated lattice structures is shown in Fig. 9. The slope of the stretch-dominated structures in both Figures 9a and 9b is n and m=1, while the slope of the bending-dominated structures is 2 (n=2) for relative stiffness (Fig. 9.a) and 1.5 (m=1.5) for relative strength (Fig. 9.b). These charts are helpful in predicting the mechanical response of lattice structures.

Fig. 9 also shows data extracted from the literature literature (Bobbert et al., 2017; Čapek et al., 2016; Dhiman et al., 2021; Liao et al., 2021; Liu et al., 2018; Ma et al., 2020, 2019; Yan et al., 2014; Yu et al., 2020; Zhao et al., 2020) for different structures and materials, as well as the results of the current study. The geometrical features and dimensions of the strut are the most significant factors affecting the mechanical behavior of lattice structures, regardless of the materials used (Zhao et al., 2016). The results indicate that most of the lattice structures fabricated in the literature fall below the ideal dominated line. Although these structures have the advantage of low relative modulus, they have lower strength and efficiency, and reach the ideal bending-dominated performance line in terms of strength. In contrast, the results of the present work, represented by the purple symbols, lie on the bending-dominated ideal for stiffness and the stretch-dominated ideal for strength. This behavior combines the advantages of low stiffness and high strength, making it a promising approach for designing architected structure implants.

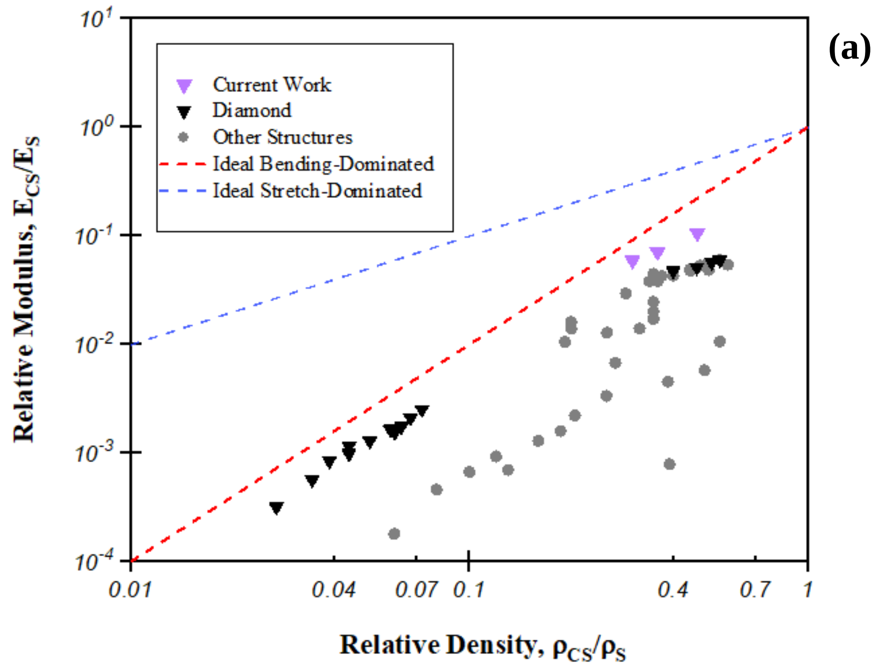

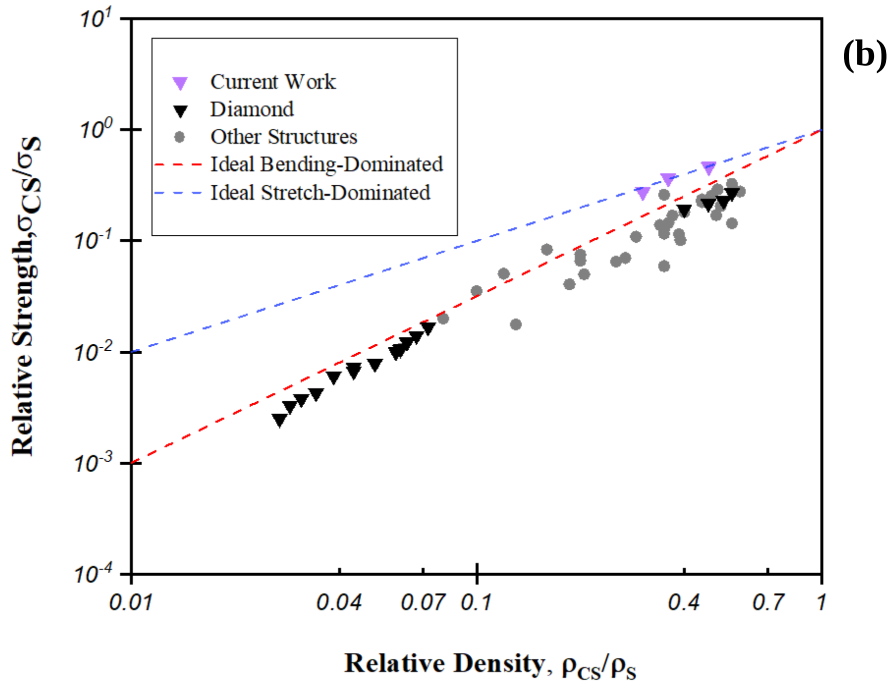

Figure 9. Relative modulus (a) and relative strength (b) plotted against relative density on logarithmic scales for irregular TPMS Diamond lattice structures of the current work and alternative topologies reported in the literature.

4 Conclusion:

This study was undertaken to design and fabricate irregular TPMS Diamond lattice structures as the internal architecture of load-bearing orthopedic implants and to evaluate their manufacturability, permeability, and mechanical performance. The substantial contribution of this work is to identify how inhomogeneity in pore size of these lattices can affect the critical considerations of both mass-flow and mechanical properties.

Samples with pore sizes ranging from 500 to 2000 um were successfully fabricated using the SLM technique with reasonable geometrical accuracy, Micro-CT analysis and density measurements revealed a slight trend of higher manufacturing accuracy towards the samples with larger pore sizes. Microscopic evaluations of lattices illustrated a dense structure with uniform melt pools consisting of columnar grains dominated by a fine cellular structure due to rapid solidification and a high cooling rate. In addition, permeability measurements demonstrated that mass transport performance of all lattices is entirely consistent with trabecular bone.

Mechanical testing of the fabricated lattices showed that those with higher porosity exhibited excellent strength and stiffness, with yield strengths and stiffness values matching those of natural trabecular bones. Smooth and nearly constant stress values in the plateau region of uniaxial compressive stress-strain curves of structures represent the ductile behavior of the fabricated lattices.

The study showed that the irregularity of pore sizes in fabricated lattices affects their mechanical behavior, with bending-dominated ideal behavior for stiffness and stretch-dominated ideal behavior for strength. This performance seems particularly promising for micro-architected implants because of the high strength to stiffness ratio. These findings are significant because they demonstrate that irregular TPMS Diamond lattice structures can be tailored to achieve desired mechanical properties and are promising candidates for load-bearing orthopedic implants.

The findings of this study have important implications for the design and development of architected lattice structures for use in biomedical implants and other engineering applications. The ability to tailor the mechanical properties of these structures by adjusting their topology and relative density offers significant opportunities for improving their performance and functionality.

Moreover, the ideal stretch- and bending-dominated models can provide valuable insights into the mechanical behavior of these structures and aid in their design and optimization.

Overall, the study highlights the potential of using irregular TPMS Diamond lattice structures as the internal architecture of load-bearing orthopedic implants. The findings provide insight into the manufacturability, permeability, and mechanical performance of these structures and suggest that they have great potential for use in orthopedic implant applications. Further research is needed to investigate the long-term performance and biocompatibility of these structures in vivo.

---

5 References

Aboulkhair, N.T., Simonelli, M., Parry, L., Ashcroft, I., Tuck, C., Hague, R., 2019. 3D printing of Aluminium alloys: Additive Manufacturing of Aluminium alloys using selective laser melting. Progress in Materials Science 106, 100578. https://doi.org/10.1016/J.PMATSCI.2019.100578

Abueidda, D.W., Elhebeary, M., Shiang, C.S. (Andrew), Pang, S., Abu Al-Rub, R.K., Jasiuk, I.M., 2019. Mechanical properties of 3D printed polymeric Gyroid cellular structures: Experimental and finite element study. Materials and Design 165, 107597. https://doi.org/10.1016/j.matdes.2019.107597

Ahmed, N., Barsoum, I., Haidemenopoulos, G., Al-Rub, R.K.A., 2022. Process parameter selection and optimization of laser powder bed fusion for 316L stainless steel: A review. Journal of Manufacturing Processes 75, 415–434. https://doi.org/10.1016/J.JMAPRO.2021.12.064

Al-Ketan, O., Abu Al-Rub, R.K., 2019. Multifunctional Mechanical Metamaterials Based on Triply Periodic Minimal Surface Lattices. Advanced Engineering Materials 21, 1900524. https://doi.org/10.1002/ADEM.201900524

Arabnejad, S., Burnett Johnston, R., Pura, J.A., Singh, B., Tanzer, M., Pasini, D., 2016. High-strength porous biomaterials for bone replacement: A strategy to assess the interplay between cell morphology, mechanical properties, bone ingrowth and manufacturing constraints. Acta biomaterialia 30, 345–356. https://doi.org/10.1016/J.ACTBIO.2015.10.048

Ashby, M.F., 2005. The properties of foams and lattices. Philosophical Transactions of the Royal Society A: Mathematical, Physical and Engineering Sciences 364, 15–30. https://doi.org/10.1098/RSTA.2005.1678

Ashman, R.B., Jae Young Rho, 1988. Elastic modulus of trabecular bone material. Journal of Biomechanics 21, 177–181. https://doi.org/10.1016/0021-9290(88)90167-4

Ataee, A., Li, Y., Brandt, M., Wen, C., 2018. Ultrahigh-strength titanium gyroid scaffolds manufactured by selective laser melting (SLM) for bone implant applications. Acta Materialia 158, 354–368. https://doi.org/10.1016/J.ACTAMAT.2018.08.005

Barba, D., Alabort, E., Reed, R.C., 2019. Synthetic bone: Design by additive manufacturing. Acta Biomaterialia 97, 637–656. https://doi.org/10.1016/J.ACTBIO.2019.07.049

Bobbert, F.S.L., Lietaert, K., Eftekhari, A.A., Pouran, B., Ahmadi, S.M., Weinans, H., Zadpoor, A.A., 2017. Additively manufactured metallic porous biomaterials based on minimal surfaces: A unique combination of topological, mechanical, and mass transport properties. Acta biomaterialia 53, 572–584. https://doi.org/10.1016/J.ACTBIO.2017.02.024

Bobbert, F.S.L., Zadpoor, A.A., 2017. Effects of bone substitute architecture and surface properties on cell response, angiogenesis, and structure of new bone. Journal of Materials Chemistry B 5, 6175–6192. https://doi.org/10.1039/C7TB00741H

Čapek, J., Machová, M., Fousová, M., Kubásek, J., Vojtěch, D., Fojt, J., Jablonská, E., Lipov, J., Ruml, T., 2016. Highly porous, low elastic modulus 316L stainless steel scaffold prepared by selective laser melting. Materials science & engineering. C, Materials for biological applications 69, 631–639. https://doi.org/10.1016/J.MSEC.2016.07.027

Cartmell, S.H., Porter, B.D., García, A.J., Guldberg, R.E., 2004. Effects of Medium Perfusion Rate on Cell-Seeded Three-Dimensional Bone Constructs in Vitro. https://home.liebertpub.com/ten 9, 1197–1203. https://doi.org/10.1089/10763270360728107

Cheng, X.Y., Li, S.J., Murr, L.E., Zhang, Z.B., Hao, Y.L., Yang, R., Medina, F., Wicker, R.B., 2012. Compression deformation behavior of Ti-6Al-4V alloy with cellular structures fabricated by electron beam melting. Journal of the mechanical behavior of biomedical materials 16, 153–162. https://doi.org/10.1016/J.JMBBM.2012.10.005

Dhiman, S., Singh, M., Sidhu, S.S., Bahraminasab, M., Pimenov, D.Y., Mikolajczyk, T., 2021. Cubic lattice structures of ti6al4v under compressive loading: Towards assessing the performance for hard tissue implants alternative. Materials 14.

https://doi.org/10.3390/MA14143866

Dong, Z., Zhao, X., 2021. Application of TPMS structure in bone regeneration. Engineered Regeneration 2, 154–162. https://doi.org/10.1016/J.ENGREG.2021.09.004

Gibson, L.J., Ashby, M.F., 2014a. Cellular solids: Structure and properties, second edition. Cellular Solids: Structure and Properties, Second Edition 1–510. https://doi.org/10.1017/CBO9781139878326

Gibson, L.J., Ashby, M.F., 2014b. Cellular solids: Structure and properties, second edition. Cellular Solids: Structure and Properties, Second Edition 1–510. https://doi.org/10.1017/CBO9781139878326

Grimm, M.J., Williams, J.L., 1997. Measurements of permeability in human calcaneal trabecular bone. Journal of Biomechanics 30, 743–745. https://doi.org/10.1016/S0021-9290(97)00016-X

Gu, D.D., Meiners, W., Wissenbach, K., Poprawe, R., 2013. Laser additive manufacturing of metallic components: materials, processes and mechanisms. https://doi.org/10.1179/1743280411Y.0000000014 57, 133–164. https://doi.org/10.1179/1743280411Y.0000000014

Guo, X., Zheng, X., Yang, Y., Yang, X., Yi, Y., 2019. Mechanical behavior of TPMS-based scaffolds: a comparison between minimal surfaces and their lattice structures. SN Applied Sciences 1, 1–11. https://doi.org/10.1007/S42452-019-1167-Z/FIGURES/9

Hutmacher, D.W., 2000. Scaffolds in tissue engineering bone and cartilage. Biomaterials 21, 2529–2543. https://doi.org/10.1016/S0142-9612(00)00121-6

Insua, A., Monje, A., Wang, H.L., Miron, R.J., 2017. Basis of bone metabolism around dental implants during osseointegration and peri-implant bone loss. Journal of biomedical materials research. Part A 105, 2075–2089. https://doi.org/10.1002/JBM.A.36060

Jones, A.C., Arns, C.H., Hutmacher, D.W., Milthorpe, B.K., Sheppard, A.P., Knackstedt, M.A., 2009. The correlation of pore morphology, interconnectivity and physical properties of 3D ceramic scaffolds with bone ingrowth. Biomaterials 30, 1440–1451. https://doi.org/10.1016/J.BIOMATERIALS.2008.10.056

Karageorgiou, V., Kaplan, D., 2005. Porosity of 3D biomaterial scaffolds and osteogenesis. Biomaterials 26, 5474–5491. https://doi.org/10.1016/J.BIOMATERIALS.2005.02.002

Lee, P.D., Quested, P.N., McLean, M., 1998. Modelling of Marangoni effects in electron beam melting. Philosophical Transactions of the Royal Society of London. Series A: Mathematical, Physical and Engineering Sciences 356, 1027–1043. https://doi.org/10.1098/RSTA.1998.0207

Leng, Y., Yang, F., Wang, Q., Li, Z., Yuan, B., Peng, C., Ren, G., Wang, Z., Cui, Y., Wang, Y., Zhu, L., Liu, H., Wu, D., 2019. Material-based therapy for bone nonunion. Materials & Design 183, 108161. https://doi.org/10.1016/J.MATDES.2019.108161

Liao, B., Xia, R.F., Li, W., Lu, D., Jin, Z.M., 2021. 3D-Printed Ti6Al4V Scaffolds with Graded Triply Periodic Minimal Surface Structure for Bone Tissue Engineering. Journal of Materials Engineering and Performance 2021 30:7 30, 4993–5004. https://doi.org/10.1007/S11665-021-05580-Z

Liu, B., Wang, H., Zhang, N., Zhang, M., Cheng, C.K., 2021. Femoral Stems With Porous Lattice Structures: A Review. Frontiers in Bioengineering and Biotechnology 9, 1136. https://doi.org/10.3389/FBIOE.2021.772539/BIBTEX

Liu, F., Zhang, D.Z., Zhang, P., Zhao, M., Jafar, S., 2018. Mechanical Properties of Optimized Diamond Lattice Structure for Bone Scaffolds Fabricated via Selective Laser Melting. Materials 2018, Vol. 11, Page 374 11, 374. https://doi.org/10.3390/MA11030374

Loh, Q.L., Choong, C., 2013. Three-dimensional scaffolds for tissue engineering applications: role of porosity and pore size. Tissue engineering. Part B, Reviews 19, 485–502. https://doi.org/10.1089/TEN.TEB.2012.0437

Lore, T., Karolien, K., Jean-Pierre, K., Jan, V.H. %J A.M., 2013. Fine-structured aluminium products with controllable texture by selective laser melting of pre-alloyed AlSi10Mg powder. Acta Materialia 61, 1809–1819.

Lu, Y., Cheng, L.L., Yang, Z., Li, J., Zhu, H., 2020. Relationship between the morphological, mechanical and permeability properties of porous bone scaffolds and the underlying microstructure. PLoS ONE 15. https://doi.org/10.1371/JOURNAL.PONE.0238471

Ma, S., Tang, Q., Feng, Q., Song, J., Han, X., Guo, F., 2019. Mechanical behaviours and mass transport properties of bone-mimicking scaffolds consisted of gyroid structures manufactured using selective laser melting. Journal of the Mechanical Behavior of Biomedical Materials 93, 158–169. https://doi.org/10.1016/J.JMBBM.2019.01.023

Ma, S., Tang, Q., Han, X., Feng, Q., Song, J., Setchi, R., Liu, Ying, Liu, Yang, Goulas, A., Engstrøm, D.S., Tse, Y.Y., Zhen, N., 2020. Manufacturability, Mechanical Properties, Mass-Transport Properties and Biocompatibility of Triply Periodic Minimal Surface (TPMS) Porous Scaffolds Fabricated by Selective Laser Melting. Materials & Design 195, 109034. https://doi.org/10.1016/J.MATDES.2020.109034

Maconachie, T., Leary, M., Lozanovski, B., Zhang, X., Qian, M., Faruque, O., Brandt, M., 2019. SLM lattice structures: Properties, performance, applications and challenges. Materials & Design 183, 108137. https://doi.org/10.1016/J.MATDES.2019.108137

Meng, L.X., Yang, H.J., Ben, D.D., Ji, H.B., Lian, D.L., Ren, D.C., Li, Y., Bai, T.S., Cai, Y.S., Chen, J., Yi, J.L., Wang, L., Yang, J.B., Zhang, Z.F., 2022. Effects of defects and microstructures on tensile properties of selective laser melted Ti6Al4V alloys fabricated in the optimal process zone. Materials Science and Engineering: A 830. https://doi.org/10.1016/j.msea.2021.142294

Murr, L.E., Quinones, S.A., Gaytan, S.M., Lopez, M.I., Rodela, A., Martinez, E.Y., Hernandez, D.H., Martinez, E., Medina, F., Wicker, R.B., 2009. Microstructure and mechanical behavior of Ti–6Al–4V produced by rapid-layer manufacturing, for biomedical applications. Journal of the Mechanical Behavior of Biomedical Materials 2, 20–32. https://doi.org/10.1016/J.JMBBM.2008.05.004

Nakamura, T., Yamamuro, T., Higashi, S., Kokubo, T., Itoo, S., 1985. A new glass-ceramic for bone replacement: evaluation of its bonding to bone tissue. Journal of biomedical materials research 19, 685–698. https://doi.org/10.1002/JBM.820190608

Nguyen, H.D., Pramanik, A., Basak, A.K., Dong, Y., Prakash, C., Debnath, S., Shankar, S., Jawahir, I.S., Dixit, S., Buddhi, D., 2022. A critical review on additive manufacturing of Ti-6Al-4V alloy: Microstructure and mechanical properties. Journal of Materials Research and Technology 18, 4641–4661. https://doi.org/10.1016/j.jmrt.2022.04.055

Novak, N., Al-Ketan, O., Krstulović-Opara, L., Rowshan, R., Abu Al-Rub, R.K., Vesenjak, M., Ren, Z., 2021. Quasi-static and dynamic compressive behaviour of sheet TPMS cellular structures. Composite Structures 266, 113801. https://doi.org/10.1016/J.COMPSTRUCT.2021.113801

Pan, C., Han, Y., Lu, J., 2020. Design and optimization of lattice structures: A review. Applied Sciences (Switzerland) 10, 1–36. https://doi.org/10.3390/APP10186374

Pennella, F., Cerino, G., Massai, D., Gallo, D., Falvo D'Urso Labate, G., Schiavi, A., Deriu, M.A., Audenino, A., Morbiducci, U., 2013. A survey of methods for the evaluation of tissue engineering scaffold permeability. Annals of Biomedical Engineering 41, 2027–2041. https://doi.org/10.1007/s10439-013-0815-5

Pobloth, A.M., Checa, S., Razi, H., Petersen, A., Weaver, J.C., Chmidt-Bleek, K., Windolf, M., Tatai, A.A., Roth, C.P., Schaser, K.D., Duda, G.N., Schwabe, P., 2018. Mechanobiologically optimized 3D titanium-mesh scaffolds enhance bone regeneration in critical segmental defects in sheep. Science translational medicine 10. https://doi.org/10.1126/SCITRANSLMED.AAM8828

Rezapourian, M., Kamboj, N., Hussainova, I., 2021. Numerical study on the effect of geometry on mechanical behavior of triply periodic minimal surfaces. IOP Conference Series: Materials Science and Engineering 1140, 012038. https://doi.org/10.1088/1757-899X/1140/1/012038

Ridzwan, M.I.Z., Shuib, S., Hassan, A.Y., Shokri, A.A., Mohammad Ibrahim, M.N., 2007. Problem of stress shielding and improvement to the hip implant designs: A review. Journal of Medical Sciences 7, 460–467. https://doi.org/10.3923/JMS.2007.460.467

Rombouts, M., Kruth, J.P., Froyen, L., Mercelis, P., 2006. Fundamentals of Selective Laser Melting of alloyed steel powders. CIRP Annals 55, 187–192. https://doi.org/10.1016/S0007-8506(07)60395-3

Sanli, I., Arts, J.J.C., Geurts, J., 2016. Clinical and Radiologic Outcomes of a Fully Hydroxyapatite-Coated Femoral Revision Stem: Excessive Stress Shielding Incidence and its Consequences. The Journal of Arthroplasty 31, 209–214. https://doi.org/10.1016/J.ARTH.2015.08.037

Taniguchi, N., Fujibayashi, S., Takemoto, M., Sasaki, K., Otsuki, B., Nakamura, T., Matsushita, T., Kokubo, T., Matsuda, S., 2016. Effect of pore size on bone ingrowth into porous titanium implants fabricated by additive manufacturing: An in vivo experiment. Materials science & engineering. C, Materials for biological applications 59, 690–701. https://doi.org/10.1016/J.MSEC.2015.10.069

Townsend, P.R., Rose, R.M., Radin, E.L., 1975. Buckling studies of single human trabeculae. Journal of biomechanics 8. https://doi.org/10.1016/0021-9290(75)90025-1

Wang, X., Xu, S., Zhou, S., Xu, W., Leary, M., Choong, P., Qian, M., Brandt, M., Xie, Y.M., 2016. Topological design and additive manufacturing of porous metals for bone scaffolds and orthopaedic implants: A review. Biomaterials 83, 127–141.

https://doi.org/10.1016/J.BIOMATERIALS.2016.01.012

Yadroitsev, I., Bertrand, P., Smurov, I., 2007. Parametric analysis of the selective laser melting process. Applied Surface Science 253, 8064–8069. https://doi.org/10.1016/J.APSUSC.2007.02.088

Yan, C., Hao, L., Hussein, A., Young, P., 2015. Ti-6Al-4V triply periodic minimal surface structures for bone implants fabricated via selective laser melting. Journal of the mechanical behavior of biomedical materials 51, 61–73. https://doi.org/10.1016/J.JMBBM.2015.06.024

Yan, C., Hao, L., Hussein, A., Young, P., Raymont, D., 2014. Advanced lightweight 316L stainless steel cellular lattice structures fabricated via selective laser melting. Materials & Design 55, 533–541. https://doi.org/10.1016/J.MATDES.2013.10.027

Yánez, A., Cuadrado, A., Martel, O., Afonso, H., Monopoli, D., 2018. Gyroid porous titanium structures: A versatile solution to be used as scaffolds in bone defect reconstruction. Materials and Design 140, 21–29. https://doi.org/10.1016/j.matdes.2017.11.050

Yu, G., Li, Z., Li, S., Zhang, Q., Hua, Y., Liu, H., Zhao, X., Dhaidhai, D.T., Li, W., Wang, X., 2020. The select of internal architecture for porous Ti alloy scaffold: A compromise between mechanical properties and permeability. Materials & Design 192, 108754. https://doi.org/10.1016/J.MATDES.2020.108754

Zarei, F., Shafiei-Zarghani, A., Dehnavi, F., 2023. Manufacturability and Mechanical Assessment of Ti-6Al-4V 3D Printed Structures for Patient-Specific Implants. Iranian Journal of Science and Technology - Transactions of Mechanical Engineering 1–13. https://doi.org/10.1007/S40997-023-00664-8/METRICS

Zhao, M., Zhang, D.Z., Liu, F., Li, Z., Ma, Z., Ren, Z., 2020. Mechanical and energy absorption characteristics of additively manufactured functionally graded sheet lattice structures with minimal surfaces. International Journal of Mechanical Sciences 167, 105262. https://doi.org/10.1016/J.IJMECSCI.2019.105262

Zhao, S., Li, S.J., Hou, W.T., Hao, Y.L., Yang, R., Misra, R.D.K., 2016. The influence of cell morphology on the compressive fatigue behavior of Ti-6Al-4V meshes fabricated by electron beam melting. Journal of the mechanical behavior of biomedical materials 59, 251–264. https://doi.org/10.1016/J.JMBBM.2016.01.034

Zhou, X., Esworthy, T., Lee, S.J., Miao, S., Cui, H., Plesiniak, M., Fenniri, H., Webster, T., Rao, R.D., Zhang, L.G., 2019. 3D Printed scaffolds with hierarchical biomimetic structure for osteochondral regeneration. Nanomedicine: Nanotechnology, Biology, and Medicine 19, 58–70. https://doi.org/10.1016/j.nano.2019.04.002